An Approach for the Verification and Validation of Rotor Aerodynamics Codes Based On Free-Wake Vortex Methods

Tonio Sant [†] [*]
Phd Student
E-mail: tsant@eng.um.edu.mt

Wouter Haans [†]
Phd Student
E-mail: W.haans@lr.tudelft.nl

Gijs van Kuik [†]
Professor
E-mail: G.A.M.vankuik@lr.tudelft.nl

Gerard .J.W van Bussel [†]
Associate Professor
E-mail: G.J.W.vanBussel@lr.tudelft.nl

[†] Section Wind Energy, Faculty of Aerospace Engineering, Delft University of Technology, Kluyverweg 1, 2629 HS, Delft, The Netherlands
[*] Mechanical Engineering Department, Faculty of Engineering, University of Malta, Msida, Malta, MSD 07

Abstract   This paper presents an approach to verify and validate a newly developed free-wake lifting line vortex code to model the wake generated by a wind turbine in axial flow conditions. Although the code is intended to simulate wind turbine wakes, it may be readily applied to propellers and helicopter rotors. The Delft University of Technology model wind turbine is used for this case study. Detailed hot-film inflow measurements in the near wake and smoke visualizations of tip vortex cores are used as a basis for validating the free-wake model. A parametric analysis was carried out to investigate how different levels of blade/wake descretizations and viscous modeling influence the accuracy of the inflow results. The tip vortex locations were compared with those predicted by the vortex model. In general very good agreement was obtained. It was found that the middle sections of the blades are rather insensitive to the choice of the viscous modeling parameters. However, high sensitivity to these parameters was observed at the blade tip and root regions.

Nomenclature

a - index to represent vortex age of trailing or shed vortex filament

c - blade local chord (m)

c_0 - maximum chord of elliptical wing (m)

fr - non-dimensional radial position along blade

h - perpendicular distance of a point in the wake from a straight-line vortex filament given point (m)

i - blade station number or trailing vortex number

l - length of vortex filament (m)

m - index to represent rotor time step

n - total number of blade stations and trailing vortices per blade

$nRev$ - number of rotor revolutions to generate free-wake

r - position vector (m)

r_c - viscous core radius of vortex filament (m)

r_{ceff} - viscous core radius of vortex filament, corrected for filament strain effects (m)

t - time (s)

u_a - azimuthally averaged axial induced velocity (m/s)

$u_{a,c}$ - axial induced velocity at blade lifting line (m/s)

y - distance travelled by elliptical wing (m)

z - parameter for viscous modelling of vortex core or spanwise position along elliptical wing

C_l - derived lift coefficient

C_d - derived drag coefficient

K_v - correction factor for viscous core effects

O - rotor hub location

R - blade tip radius

Re - Reynolds number at blade section

$RCTF$ - relative computational time factor for free-wake solution

S_c - viscous core time-offset parameter (s)

U - wind tunnel speed (m/s)

V_r - flow velocity relative to blade section (m/s)

X-Y-Z - set of co-ordinates with Z pointing vertically upwards and Y aligned with the direction of undisturbed wind flow

Xa-Ya-Za - set of co-ordinates with Z pointing vertically upwards and Ya aligned with the rotor shaft

α - angle of attack (deg) or viscous core growth constant in vortex model

δ_v - viscous core diffusivity coefficient in vortex model

ε - vortex filament strain

ξ_n - relative error when varying n (%)

ξ_{fw} - relative error due to far wake (%)

ξ_{wp} - relative error for wake periodicity (%)

$\xi_{\Delta\phi}$ - relative error when varying $\Delta\phi$ (%)

ϕ - azimuth angle of blade (deg)

λ - rotor tip speed ratio

ν - kinematic viscosity of fluid (m^2/s)

θ - local blade pitch angle (deg)

τ - index to denote time step

Ψ - yaw angle (deg)

$\Delta\phi$ - rotor angular step (deg)

$\Delta\tau$ - rotor time step (s)

Ω - rotor angular speed (rad/s)

Γ - circulation (m^2/s)

Γ_{bound} - bound circulation (m^2/s)

Γ_{trail} - trailing circulation (m^2/s)

Γ_{shed} - shed circulation (m^2/s)

56.1

1.0 - Introduction

The cost-effectiveness of rotor designs is dependent on the accuracy and reliability of simulation codes modeling rotor aerodynamics. Due to its relatively high computational efficiency, a majority of aeroelastic design software still rely on the Blade-Element-Momentum (BEM) theory for predicting the aerodynamic loads on blades. However, this theory lacks the physics to mathematically model the complex flow fields around a rotor and consequently its accuracy may be unsatisfactory. CFD methods are much more comprehensive. Unfortunately, with present computer capacity, they are still too computationally expensive to be fully integrated into aeroelastic design codes.

A special class of rotor aerodynamic models that are less computationally demanding than CFD techniques but are more reliable than BEM methods, are the so-called free-wake vortex methods. These methods are based on the principle that for flows that may be assumed to be incompressible and inviscid, vorticity formed at the blades is convected into the wake as trailing and shed vorticity with a local velocity that is the vectorial sum of the free stream velocity and that induced by all vorticity sources in the wake and from the blades. These methods are typically unsteady in nature: vorticity in the wake is allowed to diffuse freely and the evolution of the wake is calculated in time. Circulation in the wake is modeled by a series of vortex filaments that may take the form of lines (refs. 1, 2, 3, 4) or particles (refs. 5,6). Circulation around the blades is modeled with a lifting line or lifting surface representation. The induced velocity at different points in the wake is computed using the Biot-Savart law. However a problem exists in calculating the induced velocities close to the vortex filaments. For points on the vortex filaments the self-induced velocity is zero, but for points moving close to a vortex filament the induced velocity will tend to infinity, according to Biot-Savart's law. So for calculating induced velocities in such points some form of de-singularisation is required. This means that if during the convective process being simulated, a vortex filament comes very close to another, it will be ejected at unrealistically high velocities. In this case, the computation diverges and the computed wake will resemble a series of "vortex spaghetti". One way of dealing with this problem is to apply a cut-off method or a viscous core model.

As with all numerical models, accurate reproduction of the results observed in the real world is an indispensable requirement. Although free-wake models have reached a reasonably good level of maturity, more rigorous validation efforts are still required. This paper describes an approach used to verify and validate a newly developed free-wake lifting-line code. Originally, the code was intended to model wind turbines but it may be readily applied to propellers and helicopter rotors. It is important to remark here the distinction between verification and validation. As defined in Ref. 10, *Verification* is the process of quantifying the numerical error in solving a conceptual model. In doing so, the accuracy of the computational solution is measured relative to two types of highly accurate solutions: analytical solutions and highly accurate solutions. *Validation*, on the other hand, is the assessment of accuracy of a computational

solution when compared with the real world, i.e. the experimental data. In verification the comparison of the computational results with the experimental data is *not* an issue. In validation this comparison *is* an issue. Briefly speaking, verification is primarily a mathematics issue while validation is a physics issue. In this study, validation is based on direct comparison of near wake inflow distributions. This makes the validation more rigorous then when comparing blade loads. The reason for this regards the basic fact that free-wake lifting line vortex methods still rely on the blade-element theory for computing the aerodynamic loads on the blades. The accuracy in load calculations will depend on the accuracy of the induced velocities computed by the free-wake code as well as the aerofoil data used. At low induction conditions however, a large error in the calculated induced velocities can still yield considerably accurate loads. But this would not mean that the free-wake model is accurate. Also errors in the aerofoil data may mask errors in the induced velocities computed by the free-wake code.

2.0 – Free-Wake Model

The free-wake model considered is specifically designed to model rotor wakes from knowledge of the aerodynamic loads at the blades. Unlike other free-wake models, it does not directly rely on the availability of aerofoil data to iteratively determine the blade loading. The input to this code is a prescribed spanwise distribution of bound circulation that may be time-dependent. From this prescription, the code will generate a wake and then calculates the 3D induced velocities at different points in the flow field of the rotor. Although the code is also applicable for yawed conditions, only axial conditions will be treated in this paper.

Model for Blade and Near Wake Fig.1 illustrates the vortex model of the rotor blades and wake. Each rotor blade is modeled as a lifting line located at the quarter chord location. The lifting line is segmented using a pre-determined number of piecewise constant vortex filaments.
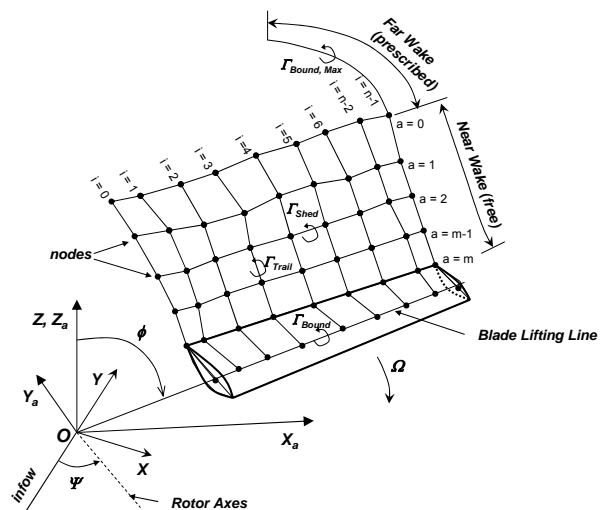

Figure 1 – Vortex model of blade, near wake and far wake.

A cosine spanwise segmentation is used to increase the number of segments at the blade tip and root, thereby increasing numerical accuracy.

The near wake is made up of vortex sheets, one for each blade. Each vortex sheet is represented by a mesh of straight-line vortex filaments which are interconnected by nodes. m is an index denoting the rotor time step while a is an index representing the vortex age. In order to keep track of all vortex filaments at each rotor time step, each node is identified by a dual numbering system is (i,a). Γ_{trail} is the circulation of each trailing vortex filament and is due to the spanwise variation in bound circulation. Γ_{shed} is the circulation of each shed vortex filament resulting from the variations of bound circulation with time. To satisfy the Kutta condition, the each wake node leaves the blades from the trailing edges, from where it advances downstream with a local velocity that is equal to the vectorial sum of the free-stream velocity and the vorticity induced velocity. The induced velocity at each node is determined using the Biot-Savart law:

$$d\vec{u} = \frac{\Gamma}{4\pi} \frac{d\vec{s} \times \vec{r}}{|\vec{r}|^3} \tag{1}$$

Viscous effects in rotor wakes are usually confined to significantly smaller scales than potential flow phenomena. However viscous effects in vortex sheets may be influential for certain operating conditions such as in blade-to-wake interactions and in skewed wakes resulting from rotor yaw. Leishman et al (Ref. 3) model viscous effects by including a parameter K_v in the Biot-Savart equation:

$$d\vec{u} = K_v \frac{\Gamma}{4\pi} \frac{d\vec{s} \times \vec{r}}{|\vec{r}|^3} \tag{2}$$

where

$$K_V = \frac{h^2}{\left(r_c^{2z} + h^{2z} \right)^{1/z}} \tag{3}$$

Equation (3) is a viscous core model in which the inner part of the vortex, denoted as the core region ($r < r_c$), almost rotates as a solid body. The outer region (outside the core, $r > r_c$) almost behaves as a potential flow. z is a constant that defines the type of velocity profile used. If z = 1, the Scully model is obtained and if z = 2, then an approximation to the Lamb-Oseen vortex model is obtained (refer to Refs. 3, 7). In this paper, the Lamb-Oseen model was used. The viscous diffusion of vorticity in this free-wake model is handled by applying a core growth model. A core growth model was adopted from Ananthan et al (Ref. 8) and is used in every trailing and shed vortex filament. The one-dimensional laminar Navier-Stokes equations reveal that the viscous vortex core radius grows with time in accordance with (Refs. 7, 8, 9):

$$r_c(t) = \sqrt{4\alpha\delta_v \upsilon t} \tag{4}$$

where α is a constant equal to 1.25643 and δ_v is the turbulent viscosity coefficient which is equal to unity in laminar flows. δ_v is added to (4) by Leishman (Ref. 9) to account for the increased vorticity diffusion in turbulent flows. Experimental investigations (Refs. 8, 9) suggest that δ_v is about 10 for small-scale rotors and is higher for full-scale rotors (on the order 100 to 1000). Current research intends to develop relations for δ_v. The following relation is used in the subject free-wake code to increase the core radius gradually with time:

$$r_c(t) = \sqrt{4\alpha\delta_v \upsilon(t + S_c)} \tag{5}$$

In (5), t =0 refers to the moment at which a vortex is shed from the blade's trailing edge. S_c is a time-offset parameter that sets a non-zero viscous core radius for vortices that are just released from the trailing edge of each blade. This parameter is introduced because viscous effects at the blades' trailing edge are non-zero and a boundary layer is present. Each vortex sheet in the free-wake model should therefore model a thickness here within which viscous effects are considerable.

Apart from viscous core growth, vorticity diffusion is also influenced by the deformation of the vortex sheet under the action of the 3D induced velocities in the wake. In a free-wake solution the wake nodes are allowed to convect freely, thereby causing the vortex filaments to be strained. This results in a change in the vorticity content of the individual filaments which in turn modifies the induced velocity field around the vortex core. To include this effect of filament straining, the core radius estimated by (5) is corrected using:

$$r_{c_{eff}} = r_{c_0} \left(\frac{1}{\sqrt{1+\varepsilon}} \right) \tag{6}$$

Where ε is the vortex filament strain. The derivation of (6) may be found in Ref. 8 and is based on Helmotz's third law stating that the net strength of a vortex should remain constant.

Model for Far Wake In order to cater for the influence of the far-field on the near wake development, a far-wake model is included. It consists of a helical tip vortex at each blade to represent fully rolled up tip vortices. Each helix is attached to the outboard corner node of the near wake vortex sheet, i.e. to node $(n-1,0)$ (refer to fig. 1). The helices extend downstream with prescribed pitch and number of rotations. The circulation of each helix is set equal to the maximum bound circulation of the corresponding blade. The helices are segmented into straight line vortex filaments and the standard Biot-Savart law (1) is applied with a simple numerical cut-off method. The number of straight line vortex segments per helical 360^0 rotation is equal to the number of time steps for the rotor to complete one whole revolution.

Numerical Solution Procedure Initially, a whole rotor revolution is sub-divided into a fixed number of equally-spaced azimuth positions. A bound circulation distribution (which is an input to the code) is prescribed at each blade for each azimuth position. The total number of time steps (M_{tot}) is then inputted. The number of rotor revolutions ($nRev$) to complete the whole solution is dependent on $\Delta\phi$ and M_{tot}. The viscous modeling parameters (δ_v and S_c) are also prescribed and these remain constant throughout the whole solution. A time-marching approach is adopted with the solution started by an impulsive start of the rotor. Before starting, the first blade is set at the zero azimuth position (blade vertical pointing upwards) and there is no near wake, but only the prescribed far

wake. The rotor is then set to rotate at constant speed. At each time step, trailing and shed vortex filaments are shed from the blades' trailing edges with a circulation calculated from the spanwise and time variations of the local bound circulation. This will eventually form the near wake that will extend downstream depending on *nRev*. At each time step, the core size of each vortex each calculated from (5) and corrected for strain in accordance with (6). The 3D induced velocities at each wake node due to all bound, trailing and shed vortices are computed using the modified Biot-Savart equation (2). The absolute velocity of the wake nodes is then estimated by vectorially adding the flow free steam velocity and the local induced velocities. Before moving to the next time step, the position of the wake nodes is updated using an Euler explicit time-integrating scheme. To improve numerical accuracy and stability, the absolute velocity used in this scheme is taken to be equal to the average of the current absolute velocity and that of the previous time-step. The above process is repeated until the rotor has rotated *nRev* revolutions. During the final revolution, the Biot-Savart law (2) is used to compute the induced velocity across the whole rotor plane (or at any other plane parallel to rotorplane) at different rotor azimuth positions. For example, if *nRev* is set equal to 3, then the induced velocity computations at the plane will be carried out between revolutions 2 and 3.

3.0 – Verification & Validation Methodology

As already outlined in section 1.0, verification will quantify the errors when solving the mathematical model numerically. On the other hand, validation will assess whether the implemented mathematical model is sufficient to describe physically the real world environment. The procedures used to verify and validate the free-wake vortex model are now described.

3.1 – Verification An essential condition of a computational solution is that it should be convergent both in discretizing (*blade and wake discretization convergence*) and iterating (*iterative convergence*). Since in the subject free-wake code, the bound circulation is prescribed directly instead of determined iteratively using aerofoil data, there are no iterative procedures here. Consequently, solution convergence is only due to insufficient blade and vortex sheet (i.e. wake) discretization. Blade and wake discretization convergence implies that by systematically using a finer descretization, the solution should eventually converge asymptotically to an exact solution which is the *calculus limit*.
The blade lifting line descretization is determined by *n* alone. Increasing *n* will make blade descretization finer as it will represent more accurately the chord and twist variations along the blade span. A larger *n* will also yield a more accurate representation of the prescribed bound circulations. The descretizaton of the near wake is determined by the number of vortex filaments to make up the mesh to represent the vortex sheet/s extending downstream from the rotor plane. This discretization is dependent on modeling parameters *n*, $\Delta\phi$ and *nrev*. $\Delta\tau$ is directly related to $\Delta\phi$ ($\Delta\tau = \Delta\phi/\Omega$). For a fixed number of rotor revolutions (*nRev*), increasing *n* and using a smaller $\Delta\phi$ will increase the number of filaments, thus making the

wake descretization finer. Another parameter is the distance to which the near wake extends downstream of the rotorplane. For fixed values of *n* and $\Delta\tau$, increasing M_{tot} will make the near wake extend more downstream. The descretization of the far wake is determined by the number of straight-line segments taken to represent the prescribed number of helices.

To be physically meaningful, the required outputs from the free-vortex solution should ideally be insensitive to descretization. In verification, a convergence study is conducted by numerical experiments in which a systematic refinement is applied with one descretization parameter at a time while holding the others constant. In this way, one may determine the most appropriate values that should be assigned to the descretization parameters in order to achieve acceptable levels of numerical accuracy. Another fact that should be taken into account is computational cost. A major drawback of free-wake models is the very rapid increase in computational cost as the number of vortex filaments is increased. Compromise should therefore be reached between numerical accuracy and computational cost. It is imperative that the verification procedure demonstrates the computational expenses required to achieve the required numerical accuracy.

The higher the number of decretization parameters, the more complex the convergence study will be. Yet there is another problem that complicates things further: apart from the descretisation parameters, there are other modeling parameters that are included to make the conceptual (mathematical) model more realistic. The problem is that we do not know exactly which values for such parameters to use for a simulation. It is best to leave the choice arbitrary and to the subjective decision of code user. It is validation *not* verification that will help us identify the most realistic values to use in a simulation. There are two sets of such arbitrary parameters in the subject free-wake model: (1)Viscous core modeling parameters (δ_v and S_c) and (2)Far wake modeling parameters (cut-off parameter, prescribed pitch and number of rotations for which the helices extend downstream). In this situation, the verification procedure should check whether the *descretizaton convergence* criterion is met over a wide range of values of the arbitrary parameters.

In this verification procedure, the computed axial induced velocity at the blades is used as a basis for comparison. Apart from providing the necessary evidence of decretization convergence and correct implementation of the conceptual model, the verification process will provide insight into the numerical behavior of the code and how the different parameters will influence the results.

To verify the free-wake model, two different case studies were considered. In the first case study, the free wake code modeled a single elliptical blade rotating at a very large radius compared to its span. This approximated an elliptical wing moving linearly at constant speed. An elliptical bound circulation was prescribed to the blade and the calculated downwash was compared with that from the analytical solution which states that the

downwash is constant along the wing span and equal to (ref. 12,13):

$$u_{a,c} = -\frac{\Gamma_{B_{\max}}}{2b} \qquad (7)$$

The blade geometric and operating parameters were set as shown in table 1. The far wake model was not included in this case study.

Table 1 – Blade Geometry and Operating Condition Parameters for Elliptical Wing

Blade Geometry Parameters	
B	1
R	1000m
Blade span	10m
θ	3deg
c_0	2m
Operating Conditions	
U	0 m/s
Ω	0.1 rev/min
ρ	1.225kg/m^3

For the second case study, the verification was carried out concurrently with the validation process when modeling the Delft wind tunnel turbine. The axial induced velocities were computed for different descretization and arbitrary parameters. The disadvantage of doing verification and validation concurrently is that any errors due to insufficient numerical convergence may mask other errors when comparing with experimental data. To avoid this problem, it was assured in this study that appropriate numerical convergence was achieved before comparing with experimental data. To limit the complexity resulting from a large number of variables to be analyzed separately while maintaining the other constant, the far wake modeling parameters whether kept constant through the verification study.

3.2 – Validation

3.2.1 - Experimental Apparatus The free-wake model was validated against hot-film inflow measurements from a model turbine in the open-jet wind tunnel of Delft University of Technology. The model turbine had the specifications as shown in table 2.

Table 2 – Wind turbine geometric specifications

Number of blades	2
Airfoil section	NACA0012
Rotor radius R	0.6 m
Blade root radius	30 % of tip radius
Chord c	0.08 m (constant)
Blade length	0.42 m
Blade twist	$\theta(fr)=(6+\theta_{tip}) - 6.67(fr)$, $0.3 \le fr \le 0.9$
	$\theta(fr) = \theta_{tip}$, $0.9 < fr \le 1$

3.2.2 – Hot-film Measurements The experiments were carried out at a rotor speed and tunnel velocity of 11.65Hz and 5.5m/s, yielding a tip speed ratio of 8. The blade pitch angle was set to 2^0. This was very close the conditions for peak power (Ref. 13). The experiments

Figure 2 – The model wind turbine and open jet wind tunnel used

were carried out at different yaw angles of the rotor, but only the experimental data for non-yawed conditions will be used in this paper. A major disadvantage of using hot-films in rotor experiments is that it is physically impossible to measure the inflow directly in the rotorplane. An estimate had to be made by taking wake measurements at different planes parallel to the rotor plane both upstream and downstream. The hot-film measurements were taken at the following planes: 3.5cm, 6.0cm and 9.0cm downstream of rotorplane and 6.0cm upstream of rotorplane. For each plane, the measuring points were located at radial positions 50%R, 60%R, 70%R, 80%R, 90%R and 100%R and at azimuth increments of 15^0. At each measurement point, the axial flow velocities (perpendicular to the rotorplane) were measured every 2^0 increments of rotor azimuth angle. These yielded velocity traces as shown in Fig. 3. At each measurement point, 54 velocity traces were taken corresponding to 54 consecutive rotor revolutions and the mean velocity trace was determined. Linear interpolation was applied using the measured data at 6cm upstream and 3.5cm downstream to obtain an estimate for the axial inflow at the rotorplane. The tangential and radial components of the inflow were also measured but these were found to be small compared to the rotorspeed and were therefore discarded for this study.

The experimental axial induced velocities at each measurement plane were obtained by subtracting the measured flow velocities from the wind tunnel velocity. For every probe position within each measuring plane, the axial induced velocity at the point of blade passage was then determined from knowledge of the distinct axial velocity pattern induced by the blades with passes across the hot-film probe, as noted in Fig. 3. This pattern, which in effect is induced by the bound vorticity at the blades is characterized by an increase in the flow velocity followed by a rapid decrease. The axial induced velocity at a blade passage is taken to be equal to the average of the maximum and minimum induced velocities of the blade passage signal. The induced velocities at the blade lifting lines (i.e. within the rotorplane) ($u_{a,c}$) were estimated from linear interpolation of the induced velocities at blade passage at measuring planes 6cm upstream and 3.5 cm downstream. The azimuthally averaged axial induced velocities (i.e. the axial induced velocities averaged over an annulus for different rotor azimuth positions) (u_a) were also found for each

measurement plane. Linear interpolation was again used to estimate the azimuthally averaged induced velocities at the rotorplane. Figs. 4 and 5 illustrate the experimental axial induced velocity distributions that were used for validating the free-wake model. The figures show the mean values obtained from the different probe positions (equi-spaced at 15^0 azimuth increments) at each radius. The corresponding standard deviations are also presented.
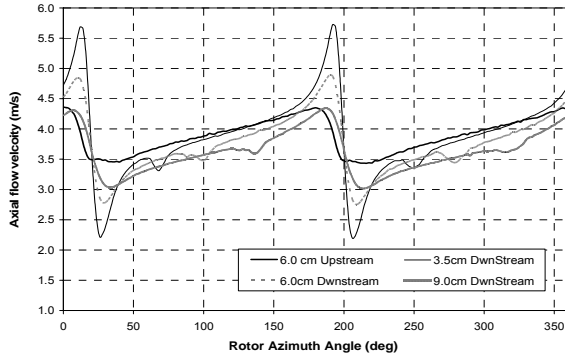

Figure 3 – Axial flow measurements taken by hot-film probe at 60%R for a whole rotor revolution. The probe position is fixed at an azimuth angle of 30 degrees.
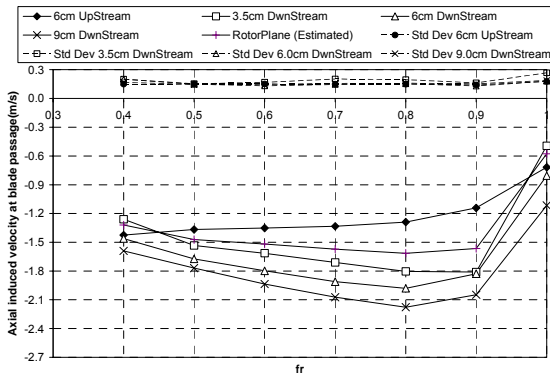
Figure 4 – Axial induced velocity distributions at blades obtained from hot-film measurements
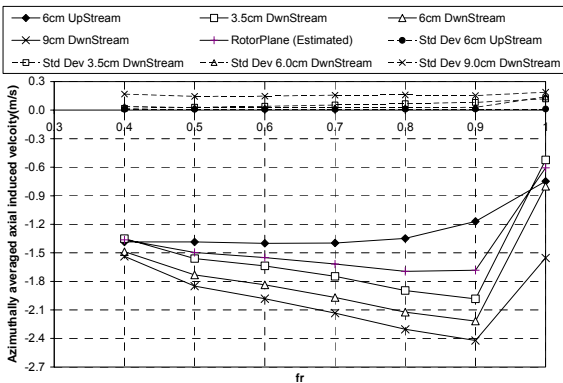
Figure 5 – Azimuthally averaged axial induced velocity distributions obtained from hot-film measurements

3.2.3 - Validation procedure using induced velocities

Once the induced velocity distributions were obtained from the experiments, the procedure described in Fig. 6 was used to validate the free-wake model:
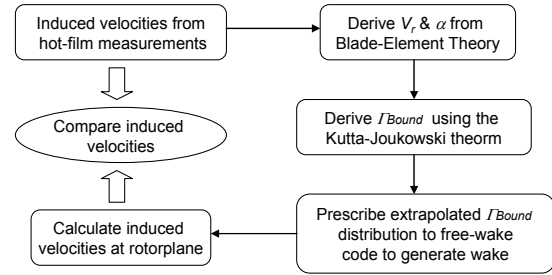
Figure 6 – Procedure for validating free-wake model using hot-film measurements

From the experimental induced velocities, the flow velocities relative to the blades (V_r) and the corresponding angles of attack (α) were found using the following blade-element theory equations for radial locations 40, 50, 60, 70, 80 and 90%R:

$$\alpha = \tan^{-1}\left(\frac{U + u_{a,c}}{r\Omega}\right) - \theta \qquad (8)$$

$$V_r = \sqrt{\left(U + u_{a,c}\right)^2 + (r\Omega)^2} \qquad (9)$$

Assuming that the flow was fully attached at all radial locations, the lift coefficient at these radial locations was found using the 2D incompressible attached flow equation given by $C_L = 2\pi\alpha$. The assumption of fully attached flow was justified since the rotor operating parameters were such that the angles of attack were small (in the range 3.6 - 8^0). The bound circulations at radial locations 40, 50, 60, 70, 80 and 90%R were estimated from the Kutta-Joukowski law :

$$\Gamma_{Bound} = \frac{1}{2}\,C_L V_r c \qquad (10)$$

The results are plotted in Fig. 7 where the points are denoted by plot 'Uncorrected'. A major difficulty encountered was to derive an extrapolated bound circulation distribution across the whole blade span from the point values at 40, 50, 60, 70, 80 and 90%R. The derived bound circulation at locations 40%R and 90%R was found to be rather unrealistically high, even though the angle of attack was derived directly from the inflow measurements. This is because these two locations are very close to the blade tip and root and the highly 3D nature of the flow here will cause the lift coefficient to be less than $2\pi\alpha$. This phenomenon has been observed by Johansen et al. (Ref. 14) when deriving lift and drag coefficients from detailed CFD computations and by Tangler (Ref. 15) when deriving aerofoil data from a pressure measurements on a rotating turbine blade using a vortex model. Three different extrapolation methods were used: In *method 1*, the estimated bound circulation values at 40, 50, 60, 70, 80 and 90%R were multiplied a the Prandtl tip and root loss equation (Ref. 18). The bound circulations at the blade root and tip (30 and 100%R) were set to zero and a linear interpolation was applied to obtain the bound circulation distribution across the whole blade (i.e. from 30 to 100%R). *Method 2* was identical to *method 1*, but with the only difference that a spline interpolation was used instead of a linear one. In *method 3*, the estimated values of the bound circulation at 40 and 90%R were discarded and a cubic variation of bound circulation was prescribed between 30 and 40%R and between 80 and 100%R. The bound circulation at 30 and 100%R was set to zero. A spline interpolation was

then applied to obtain the bound circulation distribution across the whole blade Fig. 7 shows the derived distributions obtained using the three methods. As it may be observed, the differences are not significant and mainly occur at the blade tip and root regions.
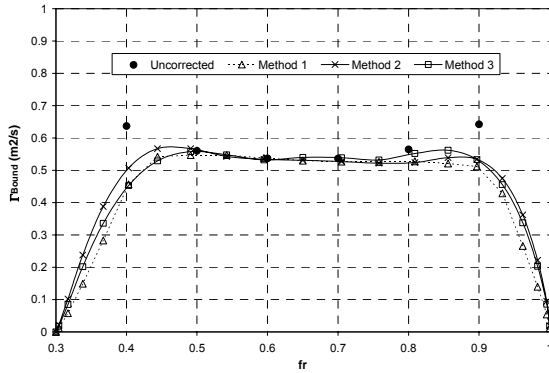

Figure 7 – Bound circulation distribution for Delft turbine as derived from hot-film wake measurements

The bound circulation distribution derived using *method 3* was used in verifying and validating the free-wake vortex code. This distribution was prescribed to the code to generate a free-wake from which a new induced velocity distribution at the rotorplane was computed and compared with the corresponding values obtained from the hot-film measurements. As a cross-check for these calculations, the local normal and tangential aerodynamic loads were computed at 50, 60, 70 and 80%R and extrapolated for the whole blade in the same way as for the bound circulation using *method 3*. The drag coefficient (C_d) was taken from the 2D NACA0012 aerofoil data. These loads distributions were then integrated to yield the power and axial thrust coefficients. The latter were then compared with those measured at the rotor shaft in the wind tunnel. The calculated results for the power and thrust coefficients were found to be equal to 0.39 and 0.71 respectively while the corresponding measured values were equal to 0.38 and 0.792 (Refs. 13, 16).

3.2.4 - Validation procedure using smoke visualization Smoke visualization experiments have also been carried out on the same model turbine to track the locations of the tip vortex cores. Further details of these experiments may be found in Ref. 16. Tip vortices in the near wake of the rotor can be seen in fig. 8. The locations of these tip vortices predicted by the free-wake model were compared with those obtained from the smoke visualization.
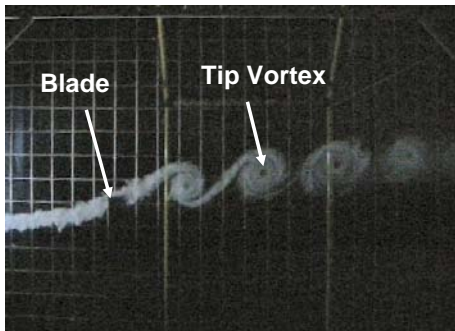

Figure 8 – Smoke visualisation photo showing tip vortex cores and the blade. Flow is from left to right.

4.0 – Results and Discussion

This section describes the results obtained from this study. The results are organized in two parts: *Part I* describes the results obtained from the verification study which modeled the elliptical wing; *Part II* describes the results from the verification and validation which modeled the wind tunnel turbine.

4.1 - Part 1: Verification by Modeling Elliptical Wing

A constant elliptical circulation distribution (time-independent) was prescribed at the blade rotating at the very large radius with Γ_{BMax} in (7) set to 10m²/s. The blade was rotated until a constant spanwise distribution for the downwash was obtained at the lifting line ($u_{a,c}$). It was found that by rotating the blade by only 3^0 was enough to yield a downwash at the lifting line that was independent of vortex sheet length. This was equivalent to ratio y/c_0 equal to about 26 where y is the distance traveled by the wing. Since the bound circulation is constant with time, there are no shed vortex filaments in the wake except those included at the first time step to account for Kelvin's condition. For Γ_{BMax} equal to 10m²/s, the analytical value for the downwash at the lifting line as given by (7) is equal to -0.5m/s.

Fig. 9 shows a typical downwash distribution predicted by the free-wake code at different values of *n*. It can be observed that the predictions are very close to the analytical result. The free-wake numerical solution predicts a downwash that is fairly constant for most of the span except at the wings tips where the downwash increases rapidly to positive values. A finer descretization for the lifting line (i.e. using a larger *n*) reduces the deviation from the analytical result at all radial locations, especially the wing tips. The discrepancies between the analytical and the free-wake code results are mainly due to the fact in the analytical solution, the wake is assumed to be rigidly flat. In the free-wake solution, the wake is allowed to develop freely in 3D space under the action of the self induced velocity and that from the blade lifting line. The resulting free wake is not flat, especially towards the wing tips were there are higher levels of trailing vorticity. Fig. 10 displays the resulting wake plot from the free-wake solution. The presence of roll-up of the vortex sheet at the wing tips is evident and the tip vortex formation at each wing tip shows up unmistakably.
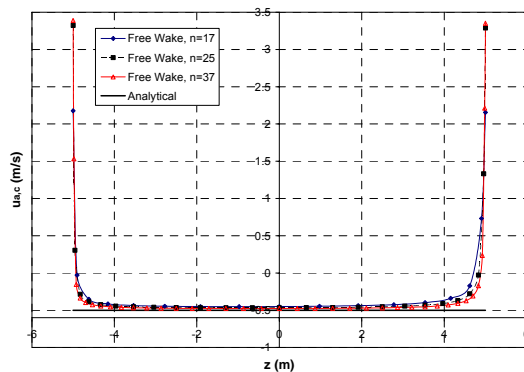

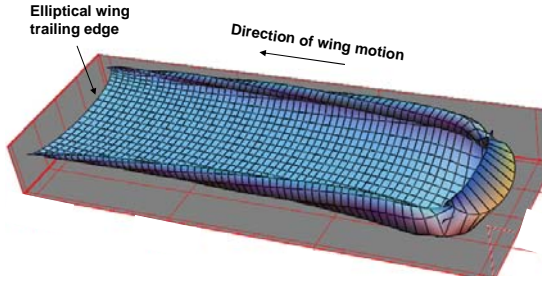*Figure 9 - Spanwise distribution of downwash for elliptical wing.*

Figure 10 – Free-wake plot for elliptical wing.

4.2 - Part 2: Verification and Validation by Modeling Wind Tunnel Turbine

The results obtained from the procedure described in sections 3.1 and 3.2 are now described. The circulation distribution of Fig. 7 (using *method 3*) was prescribed to the free-wake code and the computations were carried out for different values of *nRev*, $\Delta\phi$, *n*, δ_v and S_c. The computed axial induced velocities were compared with those obtained experimentally (Figs. 4 and 5). The wake vortical locations predicted by the free-wake code were compared with the tip vortex locations measured during the smoke visualization experiments.

To limit the number of variables in the verification and validation study, the prescribed far wake parameters (pitch, number of helical revolutions and cut-off distance) were kept constant throughout the study. To determine an appropriate pitch for the far wake, preliminary free-wake computations were carried out at different far wake pitch values and the pitch value was extracted from the computed near wake geometry. The number of helical revolutions was kept constant at 5. A constant cut-off distance of 0.5mm was used.

4.2.1 – Effect of *nRev* and far wake model

In order to obtain realistic results for the induced velocities at the blade lifting lines, one should make sure that the free-wake (i.e. the near wake in this context) extends far enough downstream from the rotor. When treating rotors in steady axial flows, two conditions must be satisfied before applying the Biot-Savart law to compute the inflow distribution at the rotorplane: *Condition 1* is that the computed induced velocity distribution at the blades should ideally be independent of the number of revolutions (*nRev*) used to generate the free-wake; *Condition 2* is that this velocity distribution should ideally be independent of the far-wake, i.e. the computed induced velocities at the rotorplane with and without the far-wake vortex model should be the same. This is because the far-wake model is only a prescribed wake vortex model and is therefore less reliable. *Condition 1* is met by selecting *nRev* large enough to reach a suitable degree of wake periodicity. Wake periodicity is achieved if, when computing the inflow at the rotorplane during the last rotor revolution, the induced velocity at the blade lifting line of the first blade at a rotor azimuth angle of 360^0 is equal to that at a rotor azimuth angle of 0^0. A suitable degree of wake periodicity is achieved if the relative error is close to zero. The percentage relative error for wake periodicity is defined here as

$$\xi_{wp} = \frac{u_{a,c}\big|_{\phi=0^0} - u_{a,c}\big|_{\phi=360^0}}{u_{a,c}\big|_{\phi=360^0}} \times 100 \tag{11}$$

Condition 2 is also met by using a sufficiently large value for *nRev*. Increasing *nRev* will push the far-wake helical vortex model away from the rotor and thus its contribution to the total induction at the blades is less influential.

In investigating quantitatively the effect of *nRev* and the far-wake, free-wake computations were computed at different values of *nRev* (equal to 1, 2, 3, 4 and 5) while keeping the other parameters, *n*, $\Delta\phi$, δ_v and S_c, constant (at 21, 10^0, 10 and 5 respectively). The reasons for selecting the latter values for such parameters will be discussed later. The induced velocities at the blades were computed with and without the far-wake model included. Note that the far wake model was still included to generate the near wake. Fig. 11 shows the computed axial induced velocity distributions at the blade lifting lines for the different *nRev* values. Fig. 12 shows the corresponding variation of the relative percentage error for wake periodicity against *nRev* computed using (11). From this figure, it may be observed that wake periodicity is achieved rapidly after the first three rotor revolutions and the percentage discrepancy converges steadily towards zero over the following revolutions. With *nRev* equal to 3, the relative percentage error is below 5 percent at all radial blade locations. Fig. 13 illustrates the increase in computational time when increasing *nRev* from 1 up to 5. The Relative Computational Time Factor (*RCTF*) is plotted here instead of the actual computational time in hours, since the latter varies depending on the computer processor speed. In this case, the *RCTF* is defined as the time required to compute the free-wake solution with a given value of *nRev* divided by the time required to do the same computation with *nRev* set to one. The rapid increase in computational time is evident from Fig. 13. Selecting *nRev* equal to 4 instead of 3 will reach a higher degree of wake periodicity but this also implies that more than double the computation time is required (*RCTF* is 36 instead of 16).
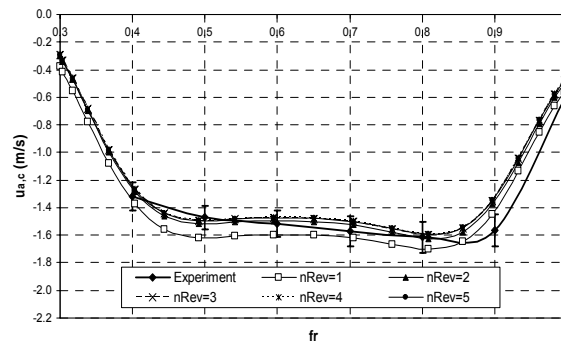

Figure 11 – Axial induced velocity distribution at blade lifting line computed by free-wake code for different values of nrev. Blade is at 360^0 azimuth. (Far wake model included in velocity calculations). Bars in experimental curve represent one +/- standard deviation in the experimental data.
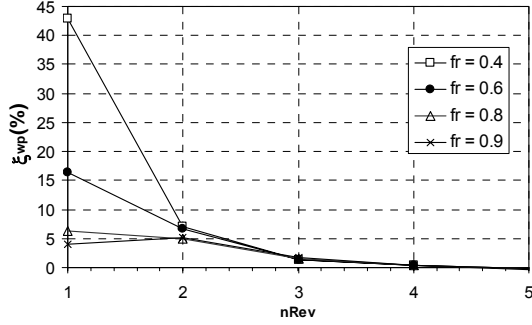
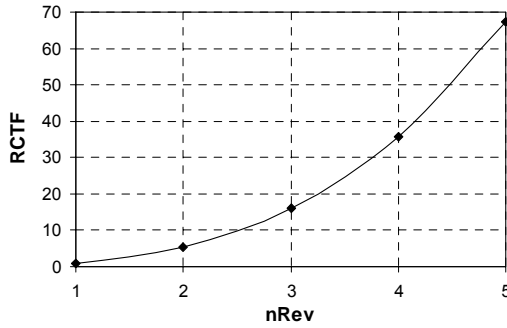*Figure 12 – Variation of Relative Percentage Error in Wake Periodicity with nRev.*

Figure 13 – Variation of Relative Computational Time Factor with nRev

Although good agreement was achieved with the experimental data when including the far wake model in the induced velocity calculations for all *nRev* (as shown in Fig. 11), the agreement was not as good when performing the same calculations excluding the far wake model (refer to Fig. 14). Yet, in Fig. 14 better agreement with the experiments is still obtained as *nRev* is increased.

In analyzing the discrepancy in calculating the induction with and without the far-wake model at different *nRev* values, the results of Figs. 11 and 14 were used to calculate the percentage relative error given by:

$$\xi_{fw} = \frac{u_{a,c}\big|_{with\ far\ wake} - u_{a,c}\big|_{without\ far\ wake}}{u_{a,c}\big|_{without\ far\ wake}} \times 100 \quad (12)$$

The errors are plotted in Fig. 15. As expected, as the number of near wake revolutions is increased, the relative error decreases and convergences steadily to approach zero. This is due to the reduced influence of the far wake on the rotorplane induction as the former is convected downstream by the growing near wake. It should be noted that at each value of *nRev*, the relative errors in Fig. 15 are significantly larger than those in Fig. 12. This implies that, as *nRev* is increased, *condition 1* (i.e. that wake periodicity is reached) is satisfied before *condition 2* (i.e. independence of far-wake model). This proves that selecting *nRev* based on satisfying *condition 1* alone is insufficient, unless *condition 2* is also satisfied.

In this analysis, the criterion to meet *conditions 1* and *2* are based on *nRev* because the latter is directly related to computational cost. In this way one could obtain insight regarding the computational cost required to reach different levels of wake periodicity and far-wake independence. But one should realize the fact that this

also depends on the operating condition of the rotor, in particular the tip speed ratio (λ).A safer criterion is to base the selection on the distance the near wake should extend downstream from the rotor. The higher the tip speed ratio, the smaller is the pitch of the vortex sheet and therefore a higher *nRev* would be required to extend the near wake suitably downstream. In this sense, free-wake models request higher computational costs when modeling high tip speeds than for lower values. In this study, in which the rotor was operating at λ=8, the corresponding near wake distance from the rotorplane for *nRev* equal to 1, 2, 3, 4 and 5 are 0.33*d*, 0.75*d*, 1*d*, 1.25*d*, and 1.5*d* respectively. This verification study therefore suggests that to reach wake periodicity and wake independence with an error of less than 10% at all radial locations at the blades, the near wake should at least extend 1.25 diameters before computing the induced velocities at the blade lifting lines.
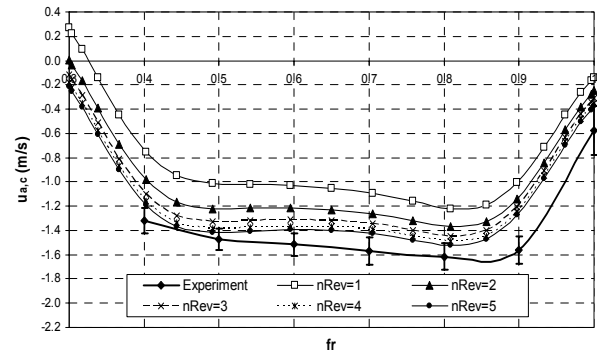

Figure 14 - Axial induced velocity distribution computed by free-wake code for different values of nRev (Far wake not included). Bars in experimental curve represent one +/- standard deviation in the experimental data.
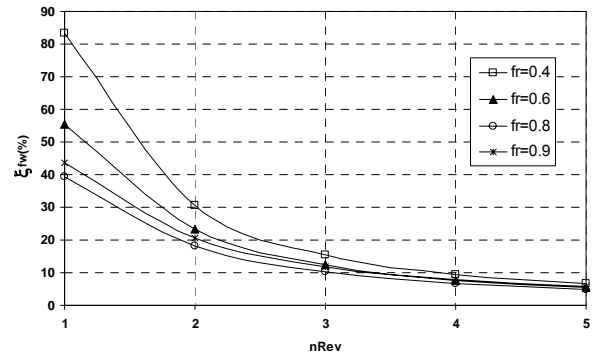

Figure 15 – Variation of Relative Percentage Error(ξ_{fw}) for discrepancies between computations for $u_{a,c}$ carried out with and without far wake model

4.2.2 – Effect of $\Delta\phi$ To investigate the influence of the time step size on the computed induced velocities at the blades, the free-wake calculations were carried out (using the bound circulation of Fig. 7, *method 3*) for different values of $\Delta\phi$, keeping the other parameters fixed. Four values for $\Delta\phi$ were chosen, equal to 7.5, 10, 15 and 30 degrees while keeping parameters *n*, *nRev*, δ_v and S_c fixed at 21, 3, 10 and 5 respectively. In these calculations, the induced velocity at the blades was computed, taking into account also the contribution from the far wake. The results are displayed in Fig. 16. The

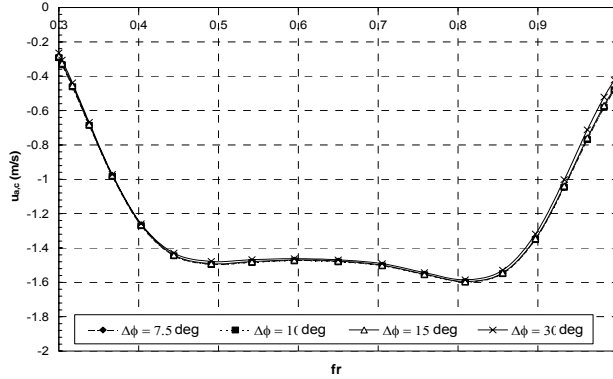differences are very small, the largest being when $\Delta\phi$ is equal to 30 degrees.

Figure 16 – Axial induced velocity distribution at blade lifting line computed by free-wake code for different values of $\Delta\phi$. Blade is at 360^0 azimuth. (Far wake model included in velocity calculations)

To quantify these differences, the relative percentage error was found using the equation:

$$\xi_{\Delta\phi} = \frac{u_{a,c}\big|_l - u_{a,c}\big|_s}{u_{a,c}\big|_s} \times 100 \tag{13}$$

where suffix s and l denote the small and large value of $\Delta\phi$ respectively. Equation (13) was applied by taking (s,l) successively equal to $(7.5^0, 10^0)$, $(10^0, 15^0)$ and $(15^0, 30^0)$. The spanwise variation of $\xi_{\Delta\phi}$ at the different values of (s,l) is shown in Fig. 17. It may be observed that the relative error is small, reaching a maximum towards the blade root and tip. $\xi_{\Delta\phi}$ becomes smaller and approaches zero as smaller values of (s,l) are used. This happens at all spanwise blade positions and provides evidence of descetization convergence in the numerical free-wake model when using gradually smaller rotor time steps.
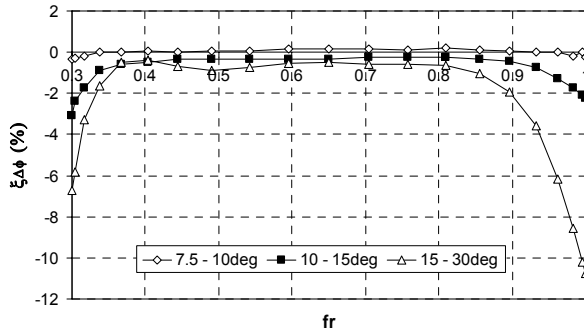
Figure 17 – Spanwise distribution of percentage relative error resulting from different values of $\Delta\phi$.

Reducing the value of $\Delta\phi$ improves numerical accuracy because it reduces the time step ($\Delta\tau$) used in the time-marching scheme. Also at a given value of $nRev$, by using smaller values for $\Delta\phi$ the wake vortices are segmented into smaller segments. This improves the accuracy with which the vortex system represents the rotor wake as discussed Gupta *et al.* (Ref. 17). Unfortunately, a reduced time step will require increased computational costs, as illustrated in Fig. 18. The *RCTF* is defined here as the time taken to carry out the free-wake with a given value of $\Delta\phi$ divided by the time taken for the same computation with $\Delta\phi$ equal to 7.5^0.
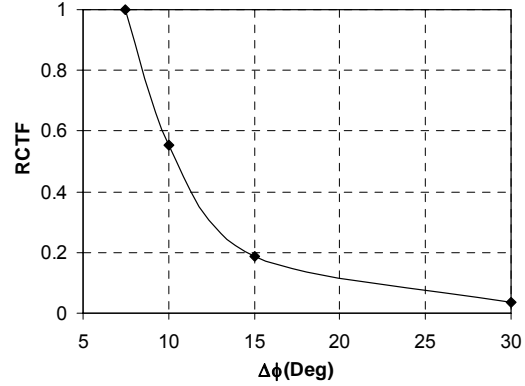

Figure 18 – Variation of Relative Computational Time Factor with $\Delta\phi$

4.2.3 – Effect of *n* and viscous modeling parameters δ_v and S_c
The free-wake calculations were also carried out at different values of *n* (equal to 11, 21 and 31) while maintaining *nRev* and $\Delta\phi$ constant (3 revolutions and 10^0 respectively). At each value of *n*, different sets of values for the viscous parameters (δ_v, S_c) were taken. The main objective of these calculations was to provide evidence of descretization convergence when increasing *n* over a wide range of value of (δ_v, S_c).

Fig. 19 shows the axial induced velocity distribution at the blade lifting line calculated for the three values of *n* with (δ_v, S_c) taken as (10,5). The presence of descretization convergence is apparent, since the discrepancy between the distributions at *n=21* and *n=31* are less than that between *n=11* and *n=21*.
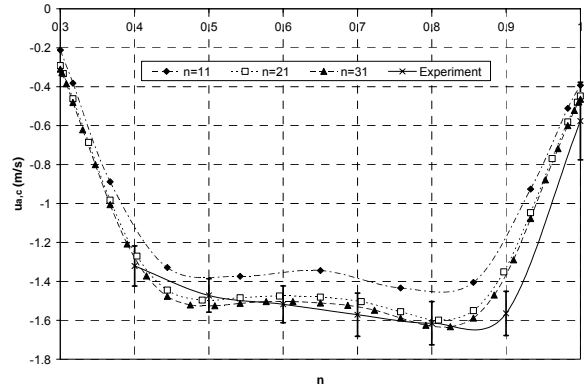

Figure 19 – Axial induced velocity distribution at blade lifting line computed by free-wake code for different values of n. (δ_v S_c) are equal to (10, 5).

The Relative Computation Time Factor (*RCTF*) variation is displayed in Fig. 20. In this case, the *RCTF* is defined as the computation time required for a given *n* value divided by that required to carry out the same computation with *n*=11. It is important to note that the computational time is not effected by the choice of (δ_v, S_c) because these parameters are not blade or wake descretization parameters. Taking *n* equal to 21 instead of 31 reduces the computational time required by about 60% and while decreasing the numerical accuracy by only a maximum of 4% at all radial locations.
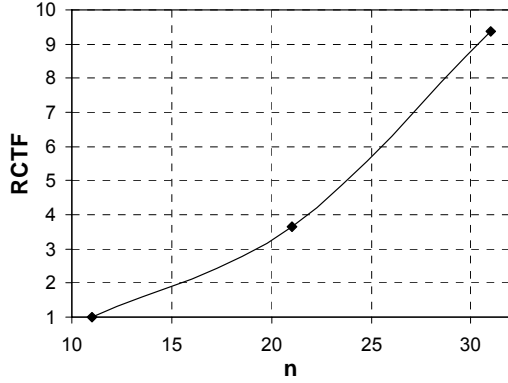
56. 10

Figure 20 – Variation of Relative Computational Time Factor with n

Relative % Error at fr=0.65	ξ_n (21,11)	ξ_n (31,21)
δ_v=10, Sc=0.1	-13.92	-5.01
δ_v=10, Sc=1	-12.79	-2.79
δ_v=10, Sc=5	-9.25	-1.99
δ_v=10, Sc=10	-8.66	-1.92

Figure 21(a) –Variation of computed Induced velocity at blade lifting line at fr=0.65 with n for different values of S_c keeping δ_v constant.(n=11, 21 and 31).

Relative % Error at fr=0.65	ξ_n (21,11)	ξ_n (31,21)
δ_v=10,Sc=10	-8.66	-1.92
δ_v=100,Sc=1	-8.74	-2.16
δ_v=10,Sc=0.1	-13.92	-5.01
δ_v=100,Sc=0.	-11.15	-3.07

Figure 21(b) –Variation of computed Induced velocity at blade lifting line at fr=0.65 with n for different values of δ_v keeping S_c constant at 10 and then at 0.1.(n=11, 21 and 31).

Figs. 21(a) and (b) illustrate how the calculated value of $u_{a,c}$ at the blade lifting line (at *fr=0.65*) varies with *n* at different values of (δ_v,S_c). Convergence was observed at all values of (δ_v,S_c). Similar convergence trends were seen at other blade spanwise locations. Higher convergence rates are achieved at larger values of δ_v and S_c. To quantify the differences in $u_{a,c}$ through varying *n*, the relative percentage error was found using the equation:

$$\xi_n = \frac{u_{a,c}\big|_l - u_{a,c}\big|_s}{u_{a,c}\big|_s} \times 100 \qquad (14)$$

where suffix *s* and *l* denote the small and large value of *n* respectively. Equation (14) was applied by taking (*s,l*) successively equal to (21,11) and (31,21) for the different values of (δ_v,S_c). Figures 21 (a) and (b) also show the resulting values of ξ_n. The decreased relative error from (21,11) to (31,21) provides evidence of numerical convergence.

After investigating the convergence trends in $u_{a,c}$ when increasing *n*, a study was then carried out to determine how different values of (δ_v,S_c) influence the correlation with the experimental data of Figs. 4 and 5. Figs. 22(a) and (b) show the spanwise distributions of the axial induced velocity at the blade lifting lines at different (δ_v,S_c). The experimental results of Figs. 4 and 5 are also included in these plots. The following observations were noted:
• Very good agreement was obtained with the experiments for the middle blade sections (from fr=0.55 to 0.75) at all (δ_v,S_c) values, except that at (100,10). In fact, at these middle sections, the calculated induced velocity is quite insensitive to values of δ_v ranging from 1 to 10 and to values of S_c ranging from 0.01 to 10 seconds.
• The agreement is not good at the blade tip and root region. High sensitivity to δ_v and S_c is observed at the blade root and tip regions.
• When assigning small values of δ_v and S_c, the induced velocity distribution will tend to a converged distribution.
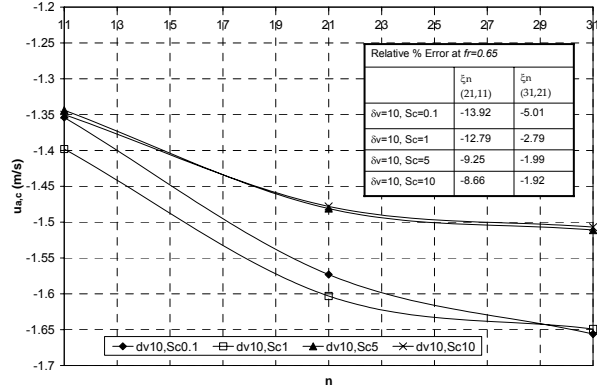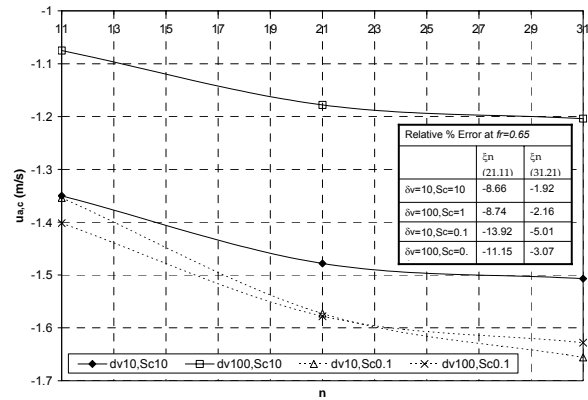
With reference to (5), increasing both δ_v and S_c increase the core radius of the viscous core filaments of the vortices that model the near wake. As it may be noted from Figs. 22(a) and (b), when assigning small values for these parameters (i.e use small core radii), the induced velocity distribution at the blade will converge to one that is very close to the real (experimental) values at the middle blade sections, but over-predicts the induced velocities at the blade tip and root. On the other hand, when assigning increasing values for δ_v and S_c, the discrepancy at the blade tip and root is reduced. But if these two parameters are increased too much, the induced velocities will reduce to unrealistic low values at all positions along the blades.

In an attempt to determine a realistic estimation of δ_v and S_c, (5) was used together with the assumption that the thickness of the viscous layer of the vortex sheet at the point when it is shed from the trailing edge of each blade is on the order of the blade thickness. This is equal to *0.12c* for the rotor considered in this case study. Based on this assumption, the core radii of the vortex filaments emerging from the blades (i.e. at *t =0*) would therefore be approximately equal to half the blade thickness. Using these criteria, equation (5) then yields that the product of δ_v X S_c equals 0.332. Given that δ_v is fixed at 10 (to follow the guidelines in Refs. 8, 9 for small-scale rotors), then S_c would be equal to 0.0332 seconds. This implies

that the axial induced velocity distribution would be somewhere between those at (10,0.01) and (10,0.1). Therefore, referring to Fig. 22(a), the distribution would have good agreement with the experimental one at the middle blade sections but not at the blade tip and root. Although there is some level of uncertainty in the computed induced velocity due to the fact that the bound circulation distribution (refer to Fig. 7) at the blade tip and root region was extrapolated (refer to section 3.2.3), one should also recall that the flow at blade tip/root regions is highly 3D in character and modeling the blade as a lifting line is insufficient here. This is a major limitation of lift-line methods, as opposed to the more accurate lifting-surface methods which cater for the 3D effects around the blade ends. The significance of the error from the lifting-line methods at the blade tip/root is dependent on the aspect ratio of the rotor blades: the higher the aspect ratio, the less is the significance of the error. For this study, the rotor blades had a low aspect ratio (equal to 5.25) and the blade root/tips were rectangular in shape. Consequently these errors are large. Luckily enough, modern wind turbine and helicopter blades have higher aspect ratios and consequently this limitation of lifting-line models is not highly influential.
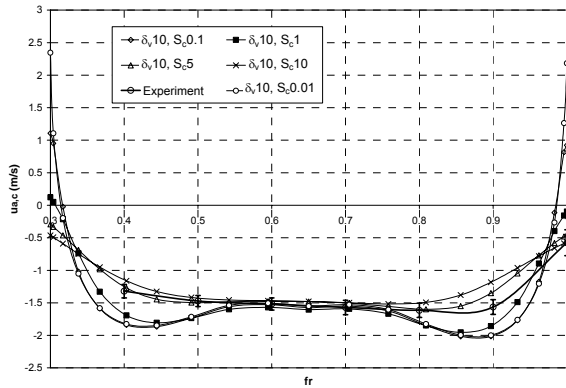
Figure 22(a) – Axial induced velocity distribution at blade lifting line computed by free-wake code for different values of S_c keeping δ_v constant.(n=21).
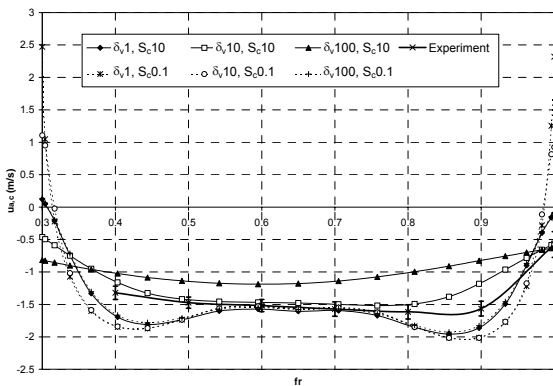

Figure 22(b) – Axial induced velocity distribution at blade lifting line computed by free-wake code for different values of δ_v keeping S_c constant at 10 and then at 0.1.(n=21).

Figures 23(a) and (b) plot the azimuthally averaged axial induced velocities at the rotorplane. This plot shows a similar behavior as for induced velocity at the lifting line, i.e. there is a low sensitivity for δ_v and S_c at the middle blade sections, but a high sensitivity at the blade tip and root regions.
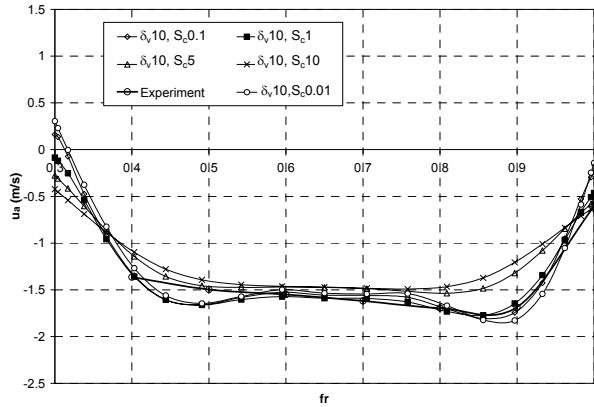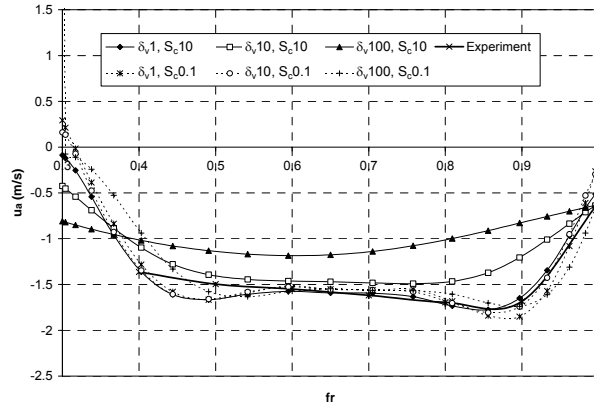

Figure 23(a) – Azimuthally-averaged axial induced velocity distribution at rotorplane computed by free-wake code for different values of S_c keeping δ_v constant.(n=21)

Figure 23(b) – Azimuthally-averaged axial induced velocity distribution at rotorplane computed by free-wake code for different values of δ_v keeping S_c constant at 10 and then at 0.1.(n=21).

In effect, δ_v and S_c determine the viscous core radius of the wake filaments at different vortex ages. The variation of the core radius with vortex age (i.e. time) at various values of δ_v and S_c may be observed in Fig. 24. S_c controls the initial core size at the point where a vortex is shed from the blade. δ_v controls the initial core size as well as the rate of core growth with time. Recall that a is an index denoting the vortex age and the lower its value, the older is the age of the vortex. It may be observed from fig. 24 that the older vortices suffer from large changes in core radius. This is because they lie on the edge of the near wake vortex sheet, close to the interface with the far wake where large filament strains are experienced. This abrupt variation is quite unrealistic and is only due to the limitation in which the wake is being modeled.
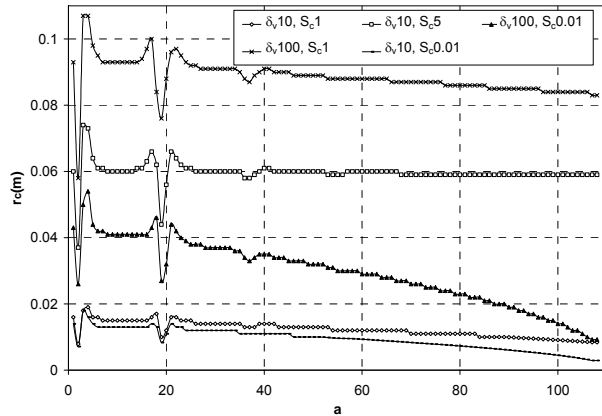
Figure 24 – Variation of viscous core radius of near wake trailing vortex filaments with vortex age at fr=0.65. (n=21,$\Delta\phi$=10^0, nRev=3)

Figs. 25(a) and (b) plot the azimuthal distribution of the axial induced velocity for *fr=0.6* and *0.9* at 3.5cm downstream from the rotorplane. The free-wake results are plotted at different viscous parameters and are compared with those measured in the wind tunnel. As a repeatability check of the experimental data, two measured traces are shown: at rotor azimuth positions 0 and 180^0, since these should be the same in a two-bladed rotor.

It may be noted in Fig. 25(a) that, although the computed induced velocity in line with the blade lifting line at *fr=0.6* agrees well with the experimental value, the comparison of the peak-to-peak velocity is not good. The peak-to-peak signal predicted by the lifting line model is only a fraction of the measured value. The main reason for this is the fact that the measured velocity signal includes the effects of a real blade section passing by. Thus the effects of section thickness and a non-zero chord length are present in the measurements. In Mast et al (Ref. 19) these effects are quantified and a method is proposed to adapt the measured velocities accordingly. As one moves away from the rotorplane, the peak-to-peak velocity predicted by the lifting line becomes more realistic. In fact, better predictions were obtained when computing the same velocity traces further downstream, at 9cm from the rotorplane (refer to figs. 26 (a) and (b)).

Fig. 27 compares the vortical wake positions predicted for different values of (δ_v,S_c) with the tip-vortex locations measured using the smoke visualization experiments (Fig. 8). It may be easily observed that for (δ_v,S_c) equal to (10,0.1), very good agreement is obtained for the wake expansion, even though such parameters did not yield an accurate prediction for the axial induced velocity at the blade root and tip (refer to Fig. 22). Recall that the selection of (10,5) resulted in a better correlation for the induced velocity at the blade root and tip. Yet this does not yield a better prediction for the wake expansion, as seen in Fig. 27(c). In effect, parameters (δ_v,S_c) control the amount of roll-up and expansion in the computed free-wake geometry. Increasing both (δ_v,S_c) reduce the wake roll-up as well as the wake expansion.

4.2.4 Wake circulation distribution - Fig. 28 illustrates the free-wake plot resulting from the bound circulation at the blades given in Fig. 7. Colour coding (shading) is introduced in the plot to denote the trailing circulation in the wake. The plot provides a better understanding of how the bound circulation at the blades is eventually diffused into the wake. The figure shows that the highest circulation occurs at the blade tip and root, with the circulation at the tip being positive, while that at the root being negative.
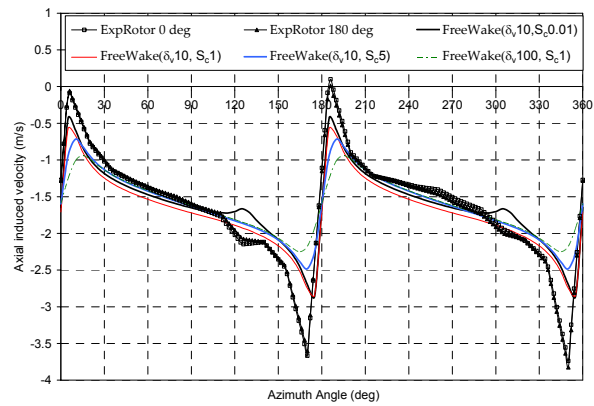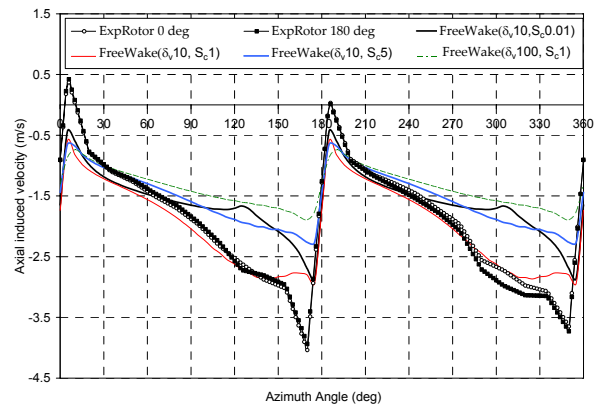

figure (a): fr = 0.6

figure (b): fr = 0.9

Figure 25 – Comparison of axial induced velocity traces computed by free-wake model with that measured by hot-film at 3.5cm downstream from rotorplane. Rotor blade is at 0/180 degrees azimuth. fig.(a): fr=0.6; fig (b): fr=0.9. (n=21,$\Delta\phi$=10^0, nRev=3)

5.0 – Conclusions

This study described an approach to verify and validate a newly-developed free-wake lifting-line vortex code for modeling rotor aerodynamics. The verification process provided insight of how different levels of blade and wake descretizations influence the accuracy of the numerical solution as well as the computational time. The validation process compared the calculated axial induced velocities at the blades and in the near wake with those obtained experimentally from hot-film measurements. This process examined how the choice of viscous modeling parameters influences the accuracy of the calculated induced velocities when comparing it with the experimental data. It was found that, for the middle blades sections, the calculated induced velocities at the blade lifting lines are quite insensitive to a wide range of values of the viscous parameters. Very good correlation with the experimental data was obtained at these middle sections. However high sensitivity to the viscous parameters was noted at the blade root/tip regions and correlation with experimental data was not good here.

This is due to the highly 3D nature of flow in these regions and is not usually catered for accurately by lifting-line blade models. Luckily, this source of inaccuracy is not very problematic when modeling blades with a high aspect ratio.
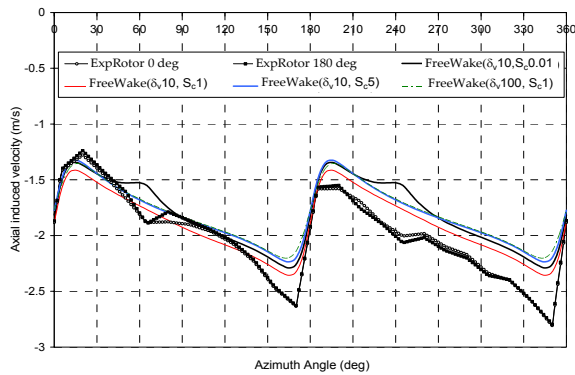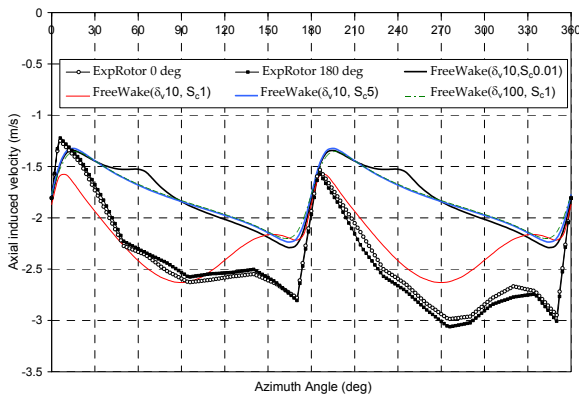

figure (a): fr = 0.6

figure (b): fr = 0.9

Figure 26 – Comparison of axial induced velocity traces computed by free-wake model with that measured by hot-film at 9cm downstream from rotorplane. Rotor blade is at 0/180 degrees azimuth. fig.(a): fr=0.6; fig (b): fr=0.9. $(n=21, \Delta\phi=10^0, nRev=3)$

Finally, the vortical locations of the free wake geometries predicted at different values of viscous modeling parameters were compared with the tip vortex locations measured using smoke visualization experiments. In general agreement was reasonably good, although it was better for those calculated using low values of the viscous parameters that correspond to smaller filament core radii. The study considered only axial conditions but in the future this work will also be extended for yawed conditions.
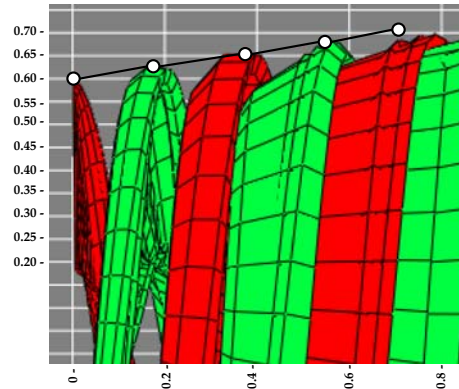
Acknowledgements
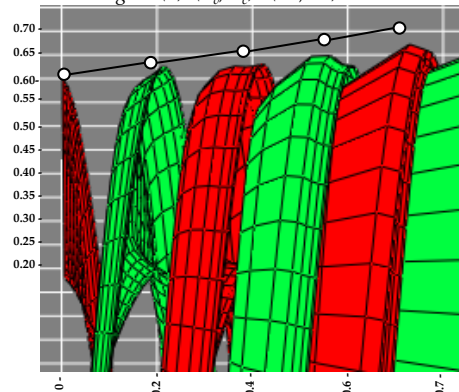
Figure (a): $(\delta_v, S_c) = (10, 0.1)$

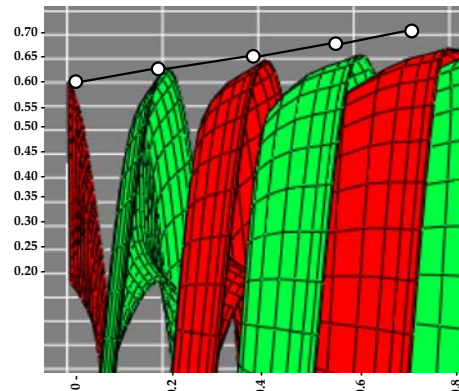Figure (b): $(\delta_v, S_c) = (10, 5)$

Figure (c): $(\delta_v, S_c) = (100, 1)$

Figure 27 – Comparison of vortical wake position computed by free-wake code at different (δ_v, S_c) with measured tip vortex locations measured using smoke visualizations (represented by white dots). $n=21, \Delta\phi=10^0, nRev=3$

References

1. Afjeh A.A. and Keith T.G. Jr., "A Simplified Free Wake Method for Horizontal-Axis Wind Turbine Performance Prediction", J*ournal of Fluids Engineering, Vol. 108, pp 400-406, 1986.*

2. Bareiß R. and Wagner S., "The Free-Wake/ Hybrid Wake Code ROLVM – A Tool for Aerodynamic Analysis of Wind Turbines," *European Wind Energy Conference, Lûbeck-Travemûnde, Germany, 1993.*

3. Leishman J.G., Bhagwat, M.J., and Bagai, A, "Free-Vortex Filament Methods for the Analysis of Helicopter Rotor Wakes", *Journal of Aircraft, Vol. 39, No. 5, pp 759-775*, 2002.
4. van Garrel, A, "Development of a Wind Turbine Aerodynamics Simulation Module", *ECN-C-03-079*, 2003.
5. Lee, D.J and Na S.U., "Numerical Simulations of Wake Structures Generated by Rotating Blades using a Time Marching Free Vortex Blob Method", *European Journal of Mechanics – B/Fluids. Vol. 18(1), 1999.*
6. Voutsinas S.G., Belessis M.A. and Huberson S., "Dynamic Inflow Effects and Vortex Particle Methods", *European Wind Energy Conference, Lûbeck-Travemûnde, Germany,* 1993.
7. J.G. Leishman, "Principles of Helicopter Aerodynamics", *Cambridge University Press*, 2002, pp 432-443.
8. Ananthan, S, Leishman J.G, Ramasamy, M, "The Role of Filament Stretching In The Free-Vortex Modelling of Rotor Wakes, *58th Annual Forum and Technology Display of the American Helicopter Society International, Montreal,* Canada, 2002.
9. Bhagwat, M.J. and Leishman J.G., "Generalized Viscous Vortex Model for Application to Free-Vortex Wake and Aeroacoustic Calculations," *58th Annual Forum and Technology Display of the American Helicopter Society International, Montreal,* Canada, 2002.
10. Oberkampf W.L. and Trucano T.G., "Verification and Validation in Computational Fluid Dynamics", *Progress in Aerospace Sciences, Vol. 38, pp 209-272, 2002.*
11. Anderson, J.D., "Fundamentals of Aerodynamics", *Third edition, McGraw-Hill, USA*, 2001, pp 331-332.
12. Katz, J. and Plotkin, A., "Low Speed Aerodynamics", *Second Edition, Cambridge University Press,* 2001,pp 173-174.
13. Vermeer, N.J., "A New Rotor Model for Aerodynamic Measurements in the Improved Open Jet Wind Tunnel", *National Wind Energy Conference, Lunteren, The Netherlands,* 1990 (in Dutch).
14. Johansen, J and SØresen N.N., "Airfoil Characteristics from 3D CFD Rotor Computations", *Proceedings of the Special Topic Conference: the Science of Making Torque from Wind*, EWEA, Delft, The Netherlands, 2004.
15. Tangler, J.L., "The Neboulous Art of Using Wind Tunnel Aerofoil Data for Predicting Rotor Performance", *Wind Energy*, Vol. 5, 2002, pp 245-257.
16. Haans W., Sant T., van Kuik G. and van Bussel G.J.W., "Measurement and Modelling of Tip Vortex Paths in the Wake of a HAWT under Yawed Flow Conditions", *Proceedings from the ASME Conference, Reno, USA,* 2005.
17. Gupta S. and Leishman J.G, "Accuracy of the Induced Velocity of Wind Turbine Wakes Using Vortex Segmentation", AIAA-2004-0828, *Proceedings from 23rd ASME Wind Energy Symposium*, Reno, 2004.
18. Sharpe D., Jenkins N., Bossanyi E. and Burton, T., "Wind Energy Handbook', *John Wiley & Sons*, 2002, pp 87.
19. Mast, E.H.M, Vermeer, L.J., Van Bussel, G.J.W., "Estimation of the Circulation Distribution on a Rotor Blade from Detailed Wake Velocities", *Wind Energy* Vol. 7, 2004, pp 189-209.
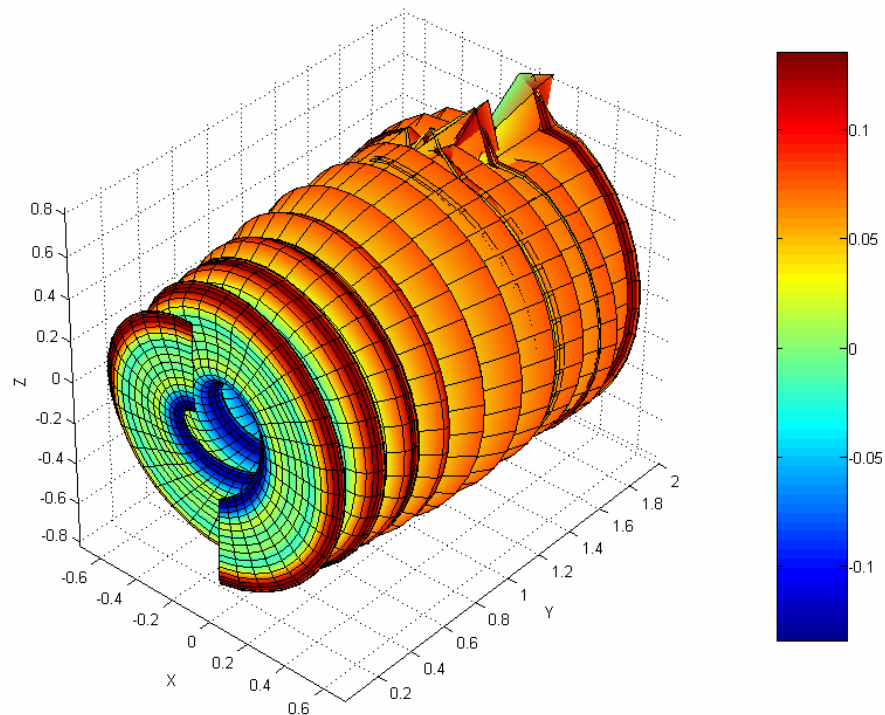
Figure 28 –Free-wake plot wit (δ_V, S_C) = (10, 5) and n=21,$\Delta\phi$=10^0, nRev=5. Color coding (shading) represents trailing circulation in wake